

A revised shape model of asteroid (216) Kleopatra

Michael K. Shepard^{a,*}, Bradley Timerson^b, Daniel J. Scheeres^c, Lance A.M. Benner^d,
Jon D. Giorgini^d, Ellen S. Howell^e, Christopher Magri^f, Michael C. Nolan^e,
Alessandra Springmann^e, Patrick A. Taylor^g, Anne Virkki^g

^a Bloomsburg University, 400 E. Second St., Bloomsburg, PA 17815, USA

^b International Occultation Timing Association, 623 Bell Rd., Newark, NY 14513, USA

^c University of Colorado, Boulder, CO 80305, USA

^d Jet Propulsion Laboratory, Pasadena, CA 91109, USA

^e Lunar & Planetary Laboratory, University of Arizona, Tucson, AZ 85721, USA

^f University of Maine Farmington, Farmington, ME 04938, USA

^g Arecibo Observatory, Universities Space Research Association, Arecibo, PR 00612, USA

ARTICLE INFO

Article history:

Received 17 October 2017

Revised 2 April 2018

Accepted 3 April 2018

Available online 6 April 2018

Keywords:

Asteroids

Asteroids, composition

Surfaces, asteroids

Radar

ABSTRACT

We used three different sets of Arecibo delay-Doppler radar images and five well-covered occultations to generate a revised three-dimensional shape model of asteroid (216) Kleopatra with a spatial resolution of ~ 10 km. We find Kleopatra to be a bi-lobate contact binary of overall dimensions $276 \times 94 \times 78$ km $\pm 15\%$ and equivalent diameter $D_{eq} = 122 \pm 30$ km; our uncertainties are upper and lower bounds. Separated binary models are ruled out by multi-chord occultations. Our model is 27% longer than the “dog-bone” model originally published by Ostro et al. (2000) but is similar to their model in the minor and intermediate axes extents. Our model's dimensions are also consistent with more recent ones based on lightcurves, adaptive-optics, and interferometric imaging. We confirm a rotational period of $P = 5.385280$ h ± 0.000001 h and a rotation pole at ecliptic longitude and latitude $(\lambda, \beta) = (74^\circ, +20^\circ) \pm 5^\circ$. Over its southern hemisphere (the one most frequently observed on Earth), Kleopatra's radar albedo is 0.43 ± 0.10 , consistent with a high near-surface bulk density and, by inference, the high metal content expected for M-class asteroids. However, the radar albedo for equatorial observations is considerably lower and more typical of a dominantly silicate composition. This observation could readily be explained by a relatively thin (1–2 m) silicate mantle over equatorial latitudes. Kleopatra's surface is relatively smooth with a mean slope of 12° at the ~ 10 km baseline scale. Analysis of its geopotential surface suggests loose material will preferentially migrate to the neck, and this is supported by our radar observations.

© 2018 Elsevier Inc. All rights reserved.

1. Introduction

Asteroid (216) Kleopatra is the second largest Tholen M-class asteroid in the solar system. Lightcurve and early radar observations (Mitchell et al., 1995 and references therein) suggested it to be a highly elongated object and possibly a close or contact binary. Adaptive-optics (AO) observations at the European Southern Observatory in 1999 suggested a close binary object (Marchis et al., 1999; Hestroffer et al., 2002a). Subsequent radar imaging observations by Ostro et al. (2000) indicated it was a contact binary and their shape model presented the community with the now iconic “dog-bone” shape. Since then, Kleopatra has been the subject of a number of investigations.

Additional Arecibo radar imaging observations of Kleopatra were acquired in 2008 and 2013. It was observed to occult stars on seven different occasions between 1980 and 2016; five were well covered with multiple chords. It has been resolved with adaptive-optics at the Canada–France–Hawaii–Telescope (CFHT) (Merline et al., 2000) and Keck (Descamps et al., 2011, 2015; Hanus et al., 2017), and observed using interferometry with the Hubble Space Telescope Fine Guidance Sensor (HST-FGS) (Tanga et al., 2001). These observations suggest that Kleopatra may be more elongated than the Ostro et al. (2000) shape model. There is still some uncertainty over whether Kleopatra is a close or contact binary.

In this paper, we use Arecibo S-band radar (2380 MHz, 12.6 cm) radar observations from 1999, 2008, and 2013, and five multi-chord stellar occultations to refine the Kleopatra shape model. In Section 2, we briefly discuss what was previously known of Kleopatra. In Section 3, we describe our methods of radar analy-

* Corresponding author.

E-mail address: msheward@bloomu.edu (M.K. Shepard).

sis and the inversion process. In Section 4, we present our results, and in Section 5 we list opportunities for future radar observations and occultations.

2. What is known of Kleopatra

2.1. Size and shape

The size most often quoted for Kleopatra is $217 \times 94 \times 81 \text{ km} \pm 25\%$ (Ostro et al., 2000) which gives an equivalent diameter (diameter of sphere with the same volume) of $D_{eq} = 109 \text{ km}$. The shape of this model is often described as a “dog bone” and consists of a long cylinder capped by two larger knobs. However, there is considerable uncertainty in both the size and shape.

Thermal infrared observations, when combined with optical photometry, allow for an estimate of optical albedo and from this, effective diameter (diameter of sphere with the same apparent cross-sectional area at some aspect). Estimates of optical albedo and diameter are $p_v = 0.11$ and $D_{eff} = 135 \pm 2 \text{ km}$ from IRAS (Tedesco et al., 2002), $p_v = 0.11$ and $D_{eff} = 138 \pm 19 \text{ km}$ from WISE (Mainzer et al., 2011), and $p_v = 0.149$ and $D_{eff} = 122 \pm 2 \text{ km}$ from the AKARI mission (Usai et al., 2011). Spitzer data in 2008 (Descamps et al., 2011) are consistent with the IRAS and WISE effective diameters. In summary, most of these data sets suggest the Ostro et al. radar-estimated size is perhaps 20% too small, although still within their 25% quoted uncertainty.

There have also been suggested refinements to the radar-derived shape model. Using AO observations from Keck, Descamps et al. (2011) describe an object $271 \times 65 \text{ km}$, with “two equal-sized misshapen lobes, each 80 km across... joined by a thin and long bridge of matter about 50 to 65 km across and 90 km long.” Similarly, interferometric observations with the HST-FGS (Tanga et al., 2001) were best modeled by two ellipsoids in contact with overall dimensions of $273 \times 75 \times 51 \text{ km}$. A summary analysis of these datasets and models by Hestroffer et al. (2002b) concluded that Kleopatra was more elongate than the radar derived shape model and specifically that the principal axis should be some 43 km longer than the Ostro et al. (2000) value (or 260 km).

Kaasalainen and Viikinkoski (2012) derive a Kleopatra shape model using 46 lightcurves, adaptive optics profiles from Descamps et al. (2011), and the HST/FGS interferometric observations of Tanga et al. (2001). Their model has similarities to those previously discussed, but they note that it was difficult to find a model that fit all the data well. They do not provide a size estimate.

Descamps (2015) used an adaptive optics image, an occultation, several lightcurves, and principles of equilibrium fluid dynamics to argue that Kleopatra’s shape is best described as a “dumb-bell,” essentially two ellipsoidal lobes connected by a thin neck with dimensions $250 \times 70 \text{ km}$ when observed in an equatorial profile.

Hanus et al. (2017) provide the most recent size and shape estimate for Kleopatra from an analysis of 55 lightcurves, 14 AO observations and 3 occultations. Their model has dimensions of $269 \times 101 \times 79 \text{ km}$ giving an equivalent diameter of $121 \pm 5 \text{ km}$, and they find a pole solution of $\sim(74^\circ, 20^\circ)$. Their model is essentially identical in dimensions to the solution we present here and can be found on the web-based Database of Asteroid Models from Inversion Techniques (DAMIT, astro.troja.mff.cuni.cz, Durech et al., 2010). We show their model alongside ours later in the paper.

2.2. Composition

The red-slope and generally featureless visible/near-infrared (VNIR) spectra of the M-class asteroids are similar to that of meteoritic iron-nickel (Fe-Ni) observed in the laboratory. One interpreta-

tion of their origin is that they are the remnant cores of ancient planetesimals exposed by cataclysmic collisions (Chapman and Salisbury, 1973; Bell et al., 1989). Additional laboratory work suggests that enstatite chondrites are also a possible analog (Gaffey, 1976; Gaffey and McCord, 1979). The recent Rosetta flyby of the M-class asteroid 21 Lutetia (Vernazza et al., 2011) supports this interpretation for at least some of the M-class.

Shepard et al. (2015) used the Arecibo radar to investigate 29 M-class asteroids because radar is a more discriminating tool than spectroscopy for the presence of metal. They found that 60% of observed M-class asteroids have radar albedos consistent with the moderate metal content of enstatite chondrite analogs, while 40% have the higher radar albedos consistent with dominantly metallic objects. The radar studies of Kleopatra to date (Mitchell et al., 1995; Magri et al., 2007a; Ostro et al., 2000) suggest it belongs to this latter group.

2.3. Mass and density

The discovery of two satellites of Kleopatra (Marchis et al., 2008, 2010; Descamps et al., 2011), subsequently named Alexhelios and Cleoselena, provide a mass estimate of $4.64 \pm 0.02 \times 10^{18} \text{ kg}$ and bulk density estimates ranging from $3.6 \pm 0.4 \text{ g cm}^{-3}$, assuming $D_{eq} = 135 \text{ km}$, to $5.4 \pm 0.4 \text{ g cm}^{-3}$, assuming $D_{eq} = 109 \text{ km}$. These bulk densities are consistent with a heavily fractured or rubble pile object composed chiefly of metal (Britt and Consolmagno, 2001; Carry, 2012).

2.4. Rotation pole and period

A number of pole estimates have been published from lightcurve analysis and AO observations; ecliptic longitude solutions cluster in the range $\lambda = 69^\circ\text{--}76^\circ$ and latitudes from $\beta = 10^\circ\text{--}25^\circ$. Mirror poles have been eliminated with the analysis of AO observations (Hestroffer et al., 2002b). The most recent pole solution by Hanus et al. (2017) is $(74^\circ, +20^\circ) \pm 5^\circ$, while Kaasalainen and Viikinkoski (2012) report $(73^\circ, +21^\circ) \pm 8^\circ$. The Ostro et al. (2000) radar-derived shape model uses a spin pole of $(\lambda, \beta) (72^\circ, +27^\circ)$.

Rotation periods derived from lightcurve analysis range from $P = 5.38326 \text{ h}$ to 5.38529 h , with the most recent (Kaasalainen and Viikinkoski, 2012; Hanus et al., 2017) estimate at 5.385280 h . We initially adopted this period, but also ran numerous models allowing it to float to determine if other periods were also reasonable. Our tests confirmed that $P = 5.385280 \text{ h}$ is the best period for our data with an uncertainty only in the last significant digit.

3. Observations

3.1. Radar background

We use the Arecibo S-band in two modes: continuous wave (or CW) and delay-Doppler. Continuous wave observations produce echo power spectra that are used to calibrate the radar reflectance properties of the target and can be used to place constraints on an object’s size, rotation period, and spin pole. Delay-Doppler observations are used to generate a two-dimensional radar “image” of the target that can be used to place strong constraints on an object’s shape.

For continuous wave radar observations, each observing cycle or “run” consists of transmission of a circularly polarized 2380 MHz (12.6 cm) signal for the round-trip light travel time to the target, followed by the reception of echoes for a similar duration in the opposite (OC) and same (SC) senses of circular polarization as transmitted. We integrate the received echo power spectra to measure the radar cross-sections of Kleopatra (in km^2) for each sense of polarization, σ_{OC} and σ_{SC} . The radar cross-section

is the cross-sectional area of a smooth, metallic sphere (a perfect isotropic reflector) that would generate the observed echo power when viewed at the same distance. Uncertainties in our estimates of absolute radar cross-section are usually $\pm 25\%$ and are based on estimates of systematic uncertainties in calibration.

We normalize the radar cross-section by the apparent cross-sectional area of the target to obtain the radar albedo. Because the OC echo is typically the strongest, the term “radar albedo” implies OC radar albedo, $\hat{\sigma}_{OC}$, unless specifically stated otherwise. It can be calculated from

$$\hat{\sigma}_{OC} = \frac{4\sigma_{OC}}{\pi D_{eff}^2}. \quad (1)$$

Published main-belt asteroid (MBA) radar albedos vary from a low of 0.039 for the CP-class 247 Eukrate (Magri et al., 2007a) to a reported maximum of 0.6 for Kleopatra (Ostro et al., 2000). The mean radar albedo for main-belt S- and C-class asteroids is $\hat{\sigma}_{OC} = 0.14 \pm 0.04$ (Magri et al., 2007a). The mean radar albedo for a sample of 29M-class asteroids is twice this and the brightest 40% of the M-class have a mean radar albedo of $\hat{\sigma}_{OC} = 0.41 \pm 0.09$, consistent with a dominantly metallic composition and regolith porosities of 30%–50% (Shepard et al., 2015).

The circular polarization ratio, μ_c , is defined to be the ratio of the SC and OC echo cross-sections:

$$\mu_c = \frac{\sigma_{SC}}{\sigma_{OC}}. \quad (2)$$

This parameter is a function of the near-surface roughness of the target. For rocky and metallic objects, values larger than zero are thought to be caused by wavelength-scale roughness in the near-surface (~ 1 m depth for 12 cm wavelength) and multiple scattering. Smooth surfaces have polarization ratios approaching 0.0, while some extremely rough surfaces have values at or even above unity (Ostro et al., 2002; Benner et al., 2008).

To generate a delay-Doppler image, we plot echo power (pixel brightness) as a function of Doppler frequency (in Hz, x -axis) and delay (in μs , y -axis). The individual images are a superposition of echoes from both hemispheres onto a plane, so they are north-south ambiguous. A convenient way of thinking about these images is to imagine looking down on the pole of the asteroid which is illuminated by a light (at the top of the image) shining on the equator of the leading hemisphere, leaving the trailing hemisphere of the asteroid in a radar shadow. Only by analyzing a number of images obtained over a sufficient range of sub-radar latitudes can the north-south ambiguity be resolved. More specific information on our methods of radar analysis can be found in Ostro et al. (2002) and Magri et al. (2007b).

3.2. Radar observations

Four different Arecibo radar data sets for Kleopatra were acquired in 1985, 1999, 2008, and 2013. The 1985 data were continuous wave (CW) only and, because they were made before the Arecibo upgrade in the mid-1990s (Campbell et al., 1997), are of lower signal-to-noise ratio (SNR) and most useful when summed. They were not used directly in the shape fit but do provide constraints on the radar albedo of Kleopatra. The other three data sets were dominated by delay-Doppler imaging and all were incorporated into our final model (Tables 1 and 2).

For the delay-Doppler radar imaging observations used in this work, we transmitted a coded signal with either 70 or 100 μs time resolution (or “baud”), corresponding to 10.5 or 15 km range resolution. We sampled the echo twice per baud (giving correlated pixels of 5.25 or 7.5 km) using the “long-code” method of Harmon (2002), and measured the echo power as a function of Doppler frequency and delay in both senses of polarization. For Kleopatra,

Table 1
Kleopatra radar encounters.

Dates	RA, DEC	Min. dist. (AU)	Sub-radar latitude
18 Nov – 01 Dec 1985	63, 11	1.162	-57°
19 Sep – 20 Nov 1999	61, 12	1.142	-57° to -60°
16–21 Sep 2008	346, 12	1.236	-12° to -13°
11 Nov – 07 Dec 2013	53, 10	1.136	-52° to -57°

Dates give the range of dates when Kleopatra was observed. RA and DEC were its Right Ascension and declination at these encounters, and Min Dist is the minimum distance to Earth during each encounter. The sub-radar latitude of Kleopatra is given at the time of the observations based on our shape model.

Table 2
Kleopatra delay-Doppler imaging.

Run	Epoch (UT)	Range res (km)	Lon ($^\circ$)
1	7 Nov 1999 04:52	7.5	30
2	7 Nov 1999 06:09	7.5	304
3	7 Nov 1999 06:45	7.5	265
4	16 Nov 1999 04:30	7.5	13
5	16 Nov 1999 05:08	7.5	331
6	16 Nov 1999 05:45	7.5	289
7	19 Nov 1999 04:38	7.5	230
8	19 Nov 1999 05:16	7.5	188
9	19 Nov 1999 05:48	7.5	152
10	20 Nov 1999 03:47	7.5	122
11	20 Nov 1999 04:25	7.5	80
12	20 Nov 1999 05:03	7.5	38
13	20 Nov 1999 05:39	7.5	358
1	16 Sep 2008 03:05	5.25	237
2	16 Sep 2008 03:46	5.25	192
3	16 Sep 2008 04:27	5.25	146
4	16 Sep 2008 05:03	5.25	106
5	18 Sep 2008 03:30	5.25	241
6	18 Sep 2008 04:12	5.25	194
7	18 Sep 2008 04:50	5.25	152
8	19 Sep 2008 02:52	5.25	118
9	19 Sep 2008 03:33	5.25	73
10	21 Sep 2008 02:44	7.5	159
11	21 Sep 2008 03:24	7.5	114
12	21 Sep 2008 05:06	7.5	68
1	11 Nov 2013 04:14	5.25	105
2	11 Nov 2013 05:30	5.25	20
3	13 Nov 2013 05:25	5.25	57
4	14 Nov 2013 04:03	5.25	344
5	14 Nov 2013 04:43	5.25	299
6	14 Nov 2013 05:21	5.25	257
7	15 Nov 2013 04:08	5.25	174
8	15 Nov 2013 04:46	5.25	132
9	15 Nov 2013 05:23	5.25	90
10	05 Dec 2013 02:10	5.25	254
11	05 Dec 2013 02:51	5.25	209
12	06 Dec 2013 02:07	5.25	93
13	06 Dec 2013 02:50	5.25	46
14	07 Dec 2013 02:03	5.25	293
15	07 Dec 2013 02:46	5.25	245

Date and time are for mid-receipt of radar echo. Range Res refers to the delay-depth of each image pixel in km. Lon refers to the sub-radar longitude of the shape model at the time of the indicated run. Sub-radar latitudes for each encounter are given in Table 1.

the delay-Doppler SC signal is so weak that we do not use it for shape modeling. While the OC SNR was suitable for radar imaging of Kleopatra, it was too low to detect satellites.

The 1999 observations provided the original shape model (Ostro et al., 2000). Given the likely pole position, these observations were at a relatively high sub-observer latitude of approximately -60° , or only a few tens of degrees from the southern pole. This aspect limited the constraints available for their final shape model and likely contributed to their underestimate of Kleopatra’s size.

The Arecibo observations acquired in 2008 were at a near-equatorial aspect and had unexpectedly low signal-to-noise ratios,

Table 3
Occultations by Kleopatra.

Date (UT)	Mid-time (UT)	Location	RA, DEC	Lat (deg)	Center Lon (deg)	Chord \pm (km)
10 Oct 1980	06:59:51	SW Canada, NW USA	349, +9	−13	201	0.8, 5.4
19 Jan 1991	05:14:21	E USA	110, +1	−35	252	1.1, 7.5
24 Dec 2009	11:58:33	SW USA	151, −6	−2	236	0.5, 3.5
12 Mar 2015	01:08:29	W Europe	168, −9	12	123	1.3, 9.2
5 Apr 2016	08:49:30	SE USA	233, −16	61	6	0.9, 6.0

Mid-time refers to the midpoint time of all observations.

Location is the general geographic region the occultation was observed.

RA,DEC are the Right Ascension and declination of the star occulted.

Lat is the sub-observer latitude (0° equatorial, +90° is N polar, etc.)

Center Lon is the sub-observer longitude on Kleopatra at occultation mid-time.

Chord \pm are estimates of the uncertainty in the chord lengths based on the apparent motion of Kleopatra and timing uncertainties of ± 0.1 s and ± 0.7 s for video and manual timing, respectively.

Details of these and other occultations by asteroids are available from NASA's Planetary Data Systems Small Bodies Node at <https://sbn.psi.edu/pds/resource/occ.html> (Dunham et al., 2016).

implying either a dramatic narrowing along the c -axis (spin axis), a radar albedo much lower than previously reported based on the 1985 and 1999 data, or some combination of both. Observations in 2013 were made at essentially the same aspect as the 1999 observations, but because of improvements to the Arecibo system in the intervening 14 years, were at a significantly higher signal-to-noise than the former.

3.3. Occultations

There have been seven observed stellar occultations by Kleopatra since 1980. Five of those have a significant number of chords (>3) and are used in our fit (Table 3) [all of the data may be found at <http://www.asteroidoccultation.com/observations/Results/> and are projected using Dave Herald's Occult software, found at <http://www.lunar-occultations.com/iota/occult4.htm>. The observers for each are listed in Table A.1]. Both radar and adaptive optics images of asteroids suffer from some degree of edge uncertainty, and final dimensions derived from these data depend critically on the radar or optical scattering model assumed and the deconvolution algorithms employed. Unlike those data sets, occultations provide sharp edges and, for this work, proved to be an essential resource for constraining the size and shape of Kleopatra.

The 1980 occultation had 11 observations and eight (8) confirmed chords, four of which were video recorded. There was also a single secondary observation which has been attributed to one of Kleopatra's satellites (Descamps et al., 2011). The 1991 occultation had nine (9) observations, eight of which confirmed an occultation, but only two of which were video recorded. The 2009 occultation had 18 observations with 13 confirmed chords, most of which were video recorded. The 2015 occultation had the greatest coverage: nearly 50 observations, mostly in Europe, and 36 confirmed chords. Finally, the 2016 occultation had 17 observations and eight (8) confirmed chords.

Uncertainties in occultation timing are not always reported and, when they are, often vary considerably. For this work, we examined those that were reported and adopt an average uncertainty of ± 0.1 s for video recorded chords and ± 0.7 s for manually timed chords. Given the relative velocity of Kleopatra for each event, we converted these into uncertainties in chord length and listed them in Table 3.

4. Analysis and results

4.1. Shape modeling

We utilized the radar SHAPE modeling software described in more detail elsewhere (Magri et al., 2007b). In essence, this software simulates the radar image or echo power spectrum for a par-

ticular model shape and compares it to the actual data. It then iteratively adjusts the parameters of the model shape and spin to minimize the chi-squared differences between synthetic and actual data. With more detailed shape models, penalty functions are available to minimize (as desired) certain features on the model, such as surface roughness or concavities. Like nearly all inverse problems, shape modeling of an asteroid may result in several reasonable solutions and other data sets become important for choosing the best. We cannot directly include the occultation data in the SHAPE algorithm, so to check the suitability of any radar-derived model, we compared the projected shapes of Kleopatra at the appropriate time with the five occultation profiles. More information on the radar inversion process and solution minimization can be found in Magri et al. (2007b).

For Kleopatra, we approached the shape inversion from two directions. On one front, we explored solutions that began with the previous (Ostro et al., 2000) shape model, while on the other we started from scratch with overlapping ellipsoid models of a variety of reasonable sizes and aspect ratios. We ran dozens of models in this way, often holding some parameters constant while allowing others to float. In this way, we looked for the best sizes, aspect ratios, radar scattering properties, spin poles, and rotation periods.

Kleopatra's odd shape ensured that the inverted rotation period was quite accurate. However, 36 years of occultation data (1980–2016) placed highly sensitive constraints on the pole direction, size, and shape that were difficult to satisfy in every case. We found numerous models that fit the radar data well and then did fine-grid (1° change) pole searches to find those most consistent with the occultations. In the end, the pole that best fit all the data is $(\lambda, \beta) = (74^\circ, +20^\circ) \pm 5^\circ$. This solution is only 7° from the (Ostro et al., 2000) pole, and essentially identical to those found by Hanus et al. (2017) and Kaasalainen and Viikinkoski (2012).

4.2. Final shape

Fig. 1 shows our best shape model along the principal axes (a – major, b – intermediate, c – minor or spin axis), and its characteristics are given in Table 4. It is best described as two ellipsoidal masses in contact with overall dimensions of $276 \times 94 \times 78$ km $\pm 15\%$ and a volume-equivalent diameter of $D_{eq} = 122 \pm 30$ km. Our listed uncertainties can be considered as upper and lower bounds (effectively three standard deviations). The a/b and a/c axial ratios of Kleopatra are 2.9 and 3.5, perhaps the highest ever measured for an object of its size (Szabo and Kiss, 2008). The two lobes are well approximated by similar tri-axial ellipsoids: one of $140 \times 79 \times 69$ km connected to another of $134 \times 90 \times 69$ km. The connecting bridge is a waist some 60 km in the b -direction and 45 km in the c -direction.

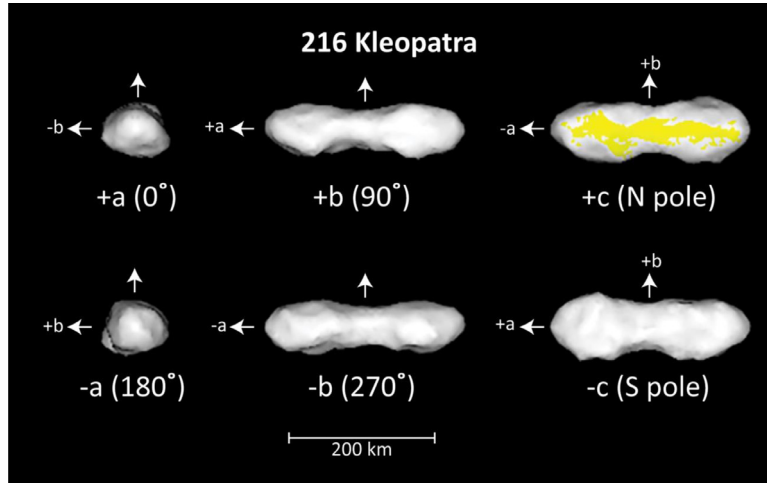


Fig. 1. Principal axis views of (216) Kleopatra along the major (a), intermediate (b), and minor (c) axes. Body-centered longitudes of each view are indicated in parentheses. The yellow (or shaded region in a non-color reproduction) in the +c view are regions where the radar view was very oblique and features are therefore less reliable. The unmarked arrows show the +c or spin-vector direction.

Table 4
Kleopatra shape model characteristics.

Maximum dimensions (km)	$276 \times 94 \times 78 \pm 15\%$
D_{eq} (km)	122 ± 30
DEEVE (km)	$310 \times 85 \times 70 \pm 15\%$
Pole (λ, β)	$(74^\circ, 20^\circ) \pm 5^\circ$
Sidereal rotation period (h)	5.385280 ± 0.000001
Surface area (km^2)	$6.223 \pm 1.320 \times 10^4$
Volume (km^3)	$9.560 \pm 2.484 \times 105$

D_{eq} is the diameter of a sphere with the same volume as the model.
DEEVE is the dynamically equivalent equal-volume ellipsoid, the ellipsoid with the same volume and moments of inertia as the model.

Fig. 2 shows the radar imaging data in three major columns, one for each date. Within each major column are three sub-columns: the left shows the raw radar image, the center column shows the simulated radar view, and the right column shows the plane of sky view for the shape model at the center time of the radar reception. The images are in chronological order of acquisition (top to bottom) and the time and date of each observation can be determined from Table 2. The arrow indicates the spin axis and the short peg marks the primary a -axis (0° body longitude). Our shape model fits the observed radar data well, but the images show some evidence for radar bright and dark regions not modeled by our simulations (we assumed a homogeneous radar albedo).

The five occultations were critical for constraining our model's size. Fig. 3 shows our and the (Ostro et al., 2000) shape models at their respective center-times. These data, especially the 2009 and 2015 occultations, effectively rule out a separated binary object. The occultations also provide hard constraints on the final model dimensions. The 2009 occultation was equatorial and 34° from a broadside view (lon 236°). The distance between the northern and southern-most chords is ~ 230 km, providing a minimum constraint on the major axis; a simplistic correction for the angle of rotation suggests a total major axis length of ~ 275 km.

The 2016 occultation had a high northern latitude view (60°) and the distance between chords suggest a minimum major axis of ~ 230 km. Applying a simplistic correction for this view gives a major axis length of ~ 266 km, consistent with the 2009 occultation analysis. This occultation also provides a minimum constraint on the width of the broader lobe b -axis of 90 km. The arrangement of the chords also hints that the two connected lobes may be canted at a small angle, similar to that observed with 25,143 Itokawa (Demura et al., 2006). We ran simulations beginning with

two lobes whose major axes were 5° to 15° offset and found no improvements in our model, but we also cannot rule it out.

The 2015 occultation had a near equatorial aspect and dense coverage of one lobe. These chords suggest a maximum c -axis (for one lobe) of 75 km, thinning to a connecting neck no wider than 50 km.

4.3. Comparisons to other models and notable features

Fig. 4 shows the Ostro et al. model, the Hanus et al. (2017) model, and ours for comparison. Both our and the Hanus et al. shape models show the intermediate axis to be wider than the short axis, *i.e.* the ellipsoids making up the two components are somewhat flattened.

Our model is generally consistent with both the size and shape found by recent AO (Descamps et al., 2011), HST-FGS observations (Tanga et al., 2002), and virtually identical in dimensions to the (Hanus et al., 2017) model. Assuming the mass estimated by Descamps et al. (2011), our model size leads to a bulk density of $4.9 \pm 0.5 \text{ g cm}^{-3}$.

Descamps (2015) describes a continuum of dumb-bell shapes using a dimensionless angular velocity parameter, Ω , which determines the ratio of waist to lobe width dimensions; lower (smaller) dimensions indicate smaller waists compared with the lobes. They find $\Omega = 0.298 \pm 0.002$ for Kleopatra, while our model, like that of Hanus et al., is more consistent with a slightly thicker waist and a previous determination by Descamps et al. (2011) of $\Omega = 0.318 \pm 0.045$.

Like most of the more recent models, ours is significantly longer in the major axis than that of Ostro et al. (2000), but is very similar in extent in the other dimensions. The disparity between the size of the original Kleopatra radar shape model and the imaging-based size estimates was explored as a function of the mechanical stability of the shape (Hirabayashi and Scheeres 2014), leveraging the fact that Kleopatra is an extreme shape and close to a fission spin rate. In that work they assumed the previous radar shape model, and scaled its length from the original shape size to the larger sizes reported by other observers (Descamps et al., 2011, Marchis et al., 2012). Since the mass was known, scaling the body length resulted in changing density, and a changing failure mode from compression (at the original scale length) to fission (at the highest scale length). Using this they found that a length scaling from 1.2 to 1.3 yielded the most stable configuration, consistent with our and other recent model estimates.

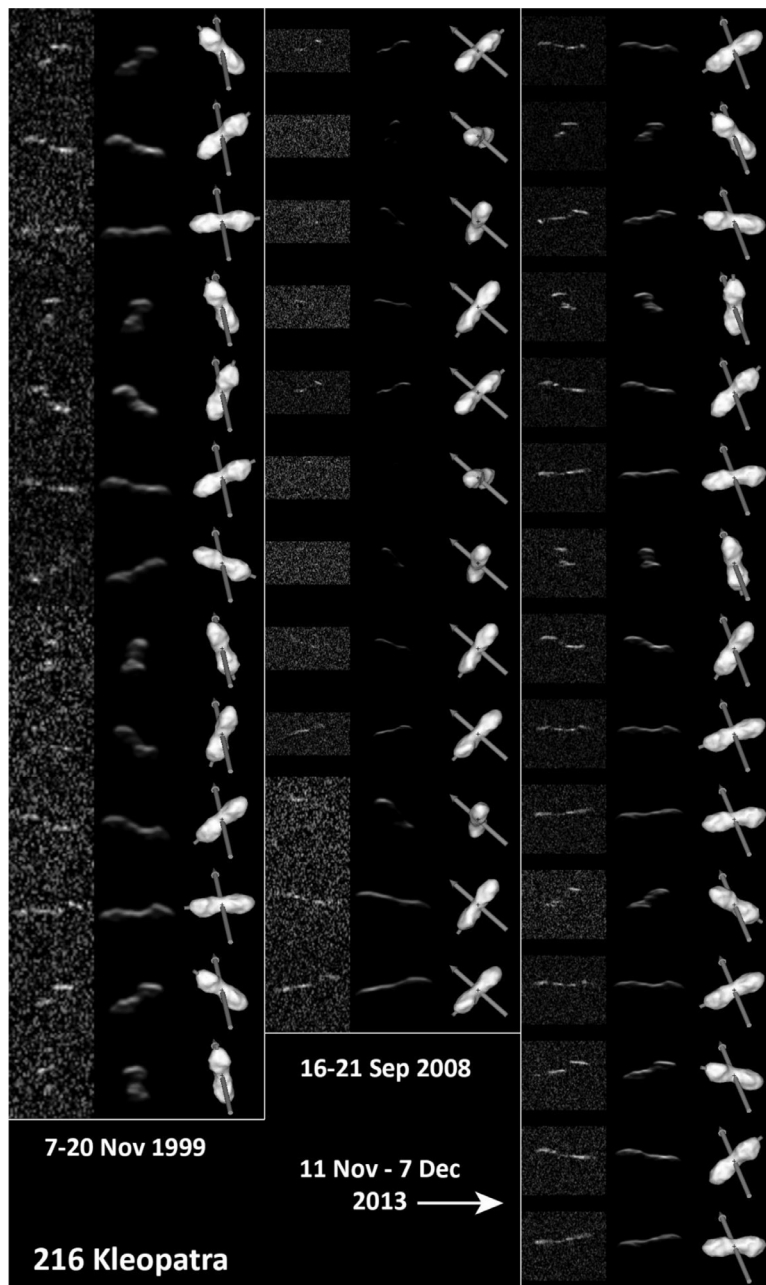


Fig. 2. Comparison of radar imaging data (left), synthetic radar data (center) and plane-of-sky view (right) for each date of delay-Doppler imaging. The rotation axis is shown as an arrow, and a peg at longitude 0° indicates the principal (major) axis of Kleopatra. The x -axis is Doppler frequency (center is 0 Hz) and the y -axis is delay depth, increasing from top to bottom. See Table 2 for dates and times (chronological order, top to bottom), delay depth, and sub-radar latitude and longitude for each image. The 1999 images are 801 Hz wide by $2050 \mu\text{s}$ high; the upper 2008 images are by 2781 Hz by $2450 \mu\text{s}$; the lower three (coarser) 2008 images are 1400 Hz by $3500 \mu\text{s}$; and the 2013 images are 1010 Hz by $2800 \mu\text{s}$.

Hanus et al. (2017) published 17 AO images that they used in their shape analysis (these may also be observed on the DAMIT website, Durech et al., 2010). Fig. 5 shows a subset of these AO images with our shape model. The views from 2008 Oct are especially useful because they are at a higher resolution. Although not used in our fit, these images appear to confirm the large-scale characteristics of our model.

There are several larger features that consistently appear in all of our better shape models (Fig. 6). The most obvious is that the anti-meridian (lon $\sim 180^\circ$) lobe is narrower than the other and asymmetric along the b -axis; mass appears to be missing on the $+b$ side (see Fig. 1, views from $+c$ or $-c$ axes, and arrow labeled A in Fig. 6).

There are two areas that appear to be relatively flat. The largest ($\sim 2500 \text{ km}^2$) is on the meridian lobe and is outlined with a dashed polygon and labeled with arrow B in Fig. 6 (see also Fig. 1, views from $+a$ and $-c$ axes). It is facing Earth when Kleopatra is centered at body lon/lat ($38^\circ, -57^\circ$) and appears to contain a shallow $\sim 20 \text{ km}$ wide depression (best seen in the far right view with arrow B). That it is flat can be surmised from the radar images on 20 Nov 1999 05:03, 11 Nov 2013 05:30, and 06 Dec 2013 02:50; all of these show a flat “head” indicating a large area of constant range (within the resolution of the pixel). The depression must be less than one range pixel, or $\sim 5 \text{ km}$, in depth, and only becomes evident when seen obliquely.

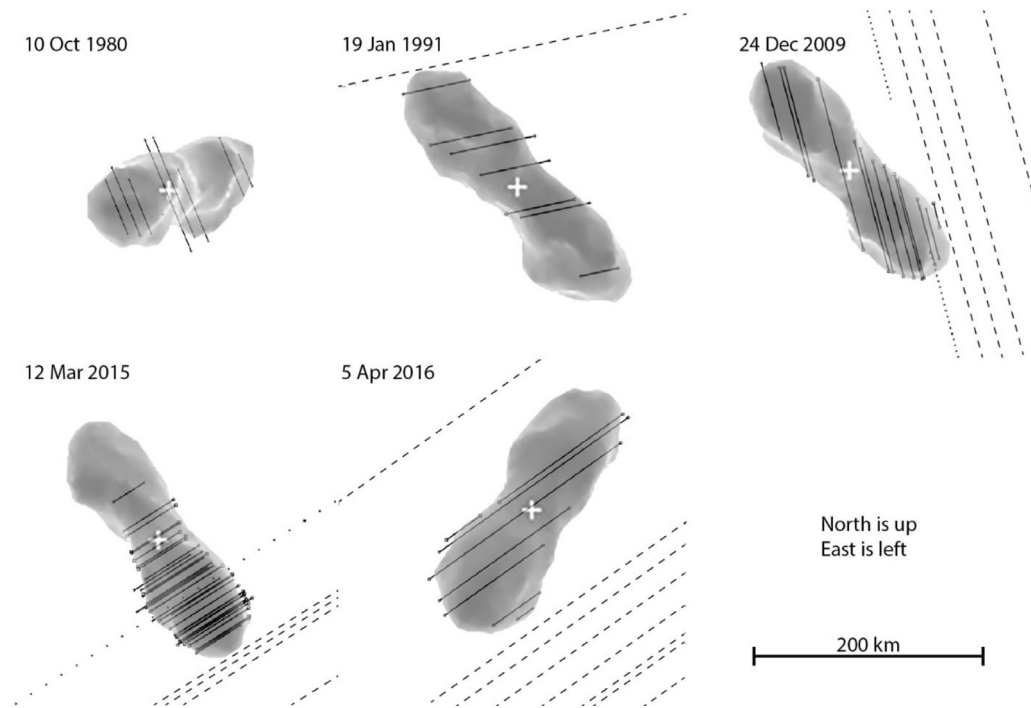


Fig. 3. (A) Plane-of-sky views of Kleopatra superimposed on chords of five well-observed occultations. The short chords are the timed observations; long, dashed chords are misses. The dotted lines in the 2009 and 2015 profiles were the original projected centerlines of the occultation (not shown on other plots). The 1980 and 1991 occultations were generally timed manually; the other dates were generally timed by video recording. The northern-most (short) chord of the 2015 occultation was not timed because of equipment malfunction, but is still shown. (B) Similar to Fig. 3A, this figure superimposes the Ostro et al. (2000) shape model over the same five occultations. This model does reasonably well with the 1980 and 2015 occultations, but is a poor fit to the other three, especially along the major axis.

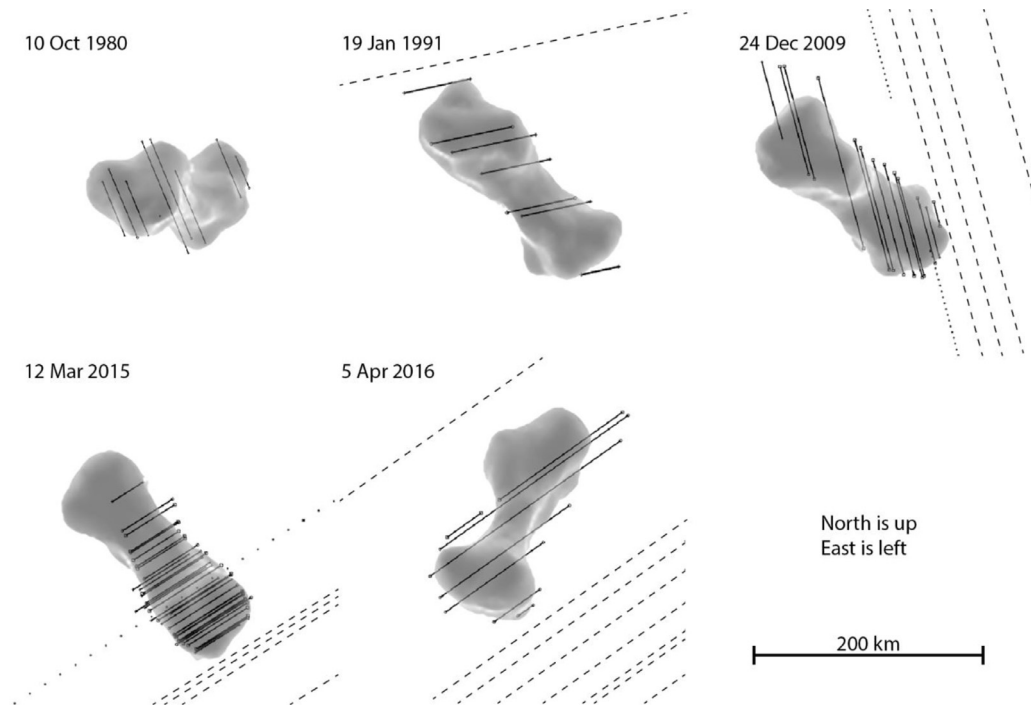


Fig. 3. Continued

The second relatively flat area is roughly half the size of the first and lies on the anti-meridian lobe (see Fig. 1, view from $-a$ axis; arrow C in Fig. 6). Like the first area, it is evident in the radar images as a group of pixels at a constant range, and is best seen in those when Kleopatra is nearly centered at lon/lat (240° , -12°), *i.e.*, those on 16 Sep 2008 03:03 and 18 Sep 2008 03:30.

Finally, the southern half of both lobes show large regions of missing mass compared with a simple triaxial ellipsoid. These regions are most evident in the $-a$ and $-b$ axis views of Fig. 1 and are indicated by arrow D in Fig. 6.

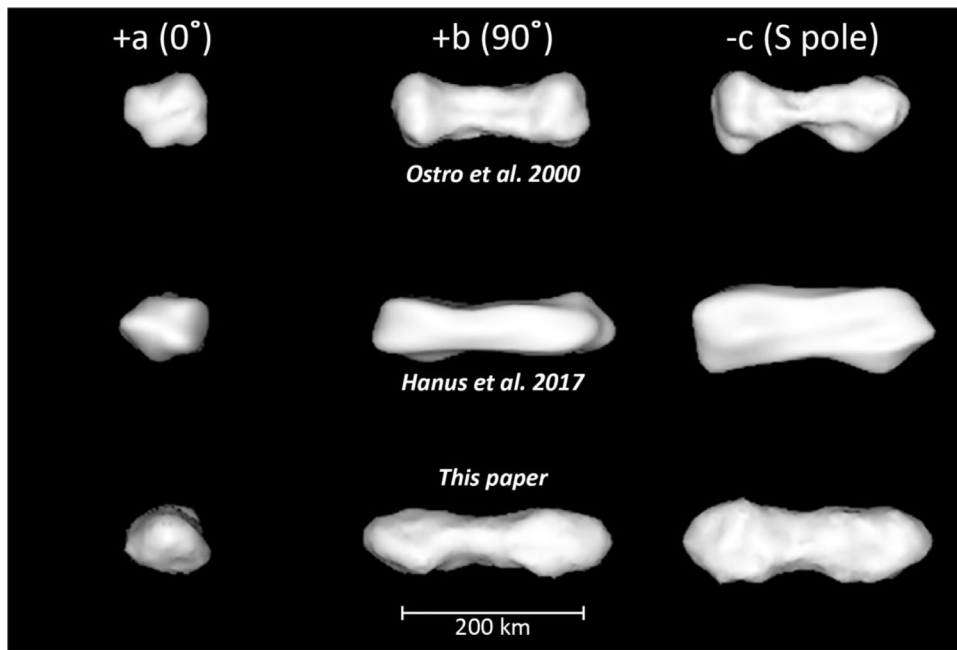


Fig. 4. Comparison of the Ostro et al. (2000) (top), Hanus et al. (2017) (middle), and our (bottom) Kleopatra shape models. Not all sides are shown.

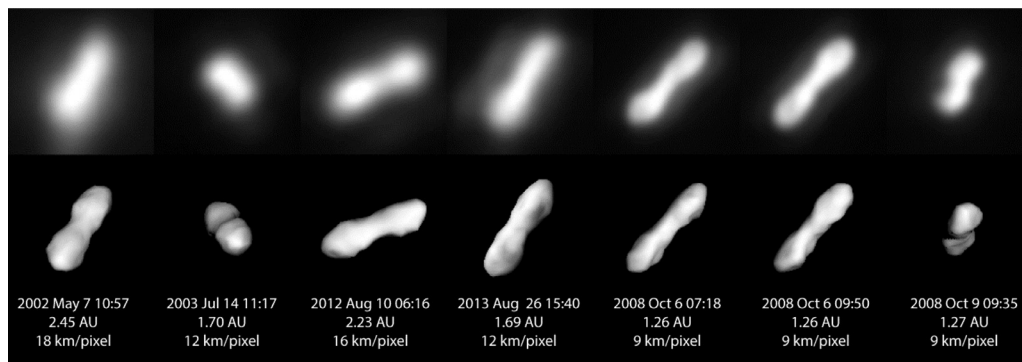


Fig. 5. A variety of the historical adaptive-optics views (Keck II NIRC2) of Kleopatra (top) compared with our predicted plane-of-sky view (center) for their respective observation times. Dates and times, distance from Earth, and original pixel-scale of the AO views are shown at the bottom. The AO views have been enlarged appropriately to match the plane-of-sky scale (350 km x 350 km, or 1.2 km/pixel). The AO images are a subsample of those used in the Hanus et al. (2017) fit (see also the Keck archive and the DAMIT entry for Kleopatra, Durech et al., 2010). References or the PI for each observation are given in Hanus et al. 2017; the 2002 PI was J. L. Margot; the 2008 PI was F. Marchis; and the 2003, 2012 and 2013 PI was W. Merline.

4.4. Radar properties

Ostro et al. (2000) reported a radar albedo of $\hat{\sigma}_{OC} = 0.60 \pm 0.30$, the highest reported radar albedo for any M-class asteroid (Shepard et al., 2015). We revise this estimate based on the accumulated observations of four radar encounters. Table 5 lists Kleopatra's CW runs for each date and the associated radar properties.

The Kleopatra radar data sets of 1985, 1999, and 2013 were all acquired at high southern latitudes, and are consistent with each other. Using our revised shape model, the radar albedo for this aspect is $\hat{\sigma}_{OC} = 0.43 \pm 0.10$, where the uncertainty listed covers the range of values observed. This value is similar to other M-class asteroids and consistent with a high surface bulk density and large metal content. The polarization ratios for most of these observations are quite low with $\mu_c \leq 0.1$, suggesting a smooth near-surface. As noted earlier, the imaging data in Fig. 3 also show that the radar albedo is inhomogeneous across the surface, a feature noted in other high albedo main-belt targets (Shepard et al., 2017).

The 2008 radar observations sharply contrast with these conspicuous echoes. The sole CW observation yields a radar albedo of $\hat{\sigma}_{OC} = 0.17 \pm 0.04$, 40% of the value indicated by the other datasets.

All of the delay-Doppler images are faint and subdued; in some images, the asteroid is only evident in a few pixels. This does not appear to be a consequence of the reduced areal cross-section of Kleopatra. It is possible that there were unknown equipment problems with the 2008 Arecibo observations, but it seems more likely that the low radar albedos are real and the result of a physical difference, *i.e.* lower surface bulk density at equatorial latitudes. A relatively thin (1–2 m) mantle of mostly silicate regolith over an otherwise metal dominated surface could create this effect.

4.5. Geophysical modeling

The geophysical environment on the surface of the revised Kleopatra shape model was investigated using techniques summarized in Scheeres (2012). The slope was computed, accounting for both rotation and gravitation, and is shown in Fig. 7. We note that the vast majority of the asteroid surface is below the usual 35° angle of repose for granular material, with the average slope being 12° and the maximum being 37° Fig. 8 shows the slope angle distribution in terms of surface area coverage. It is significant to note that the regions of highest variation in slope coincide with the imaged surface of the asteroid. The slope shows deviation from a fig-

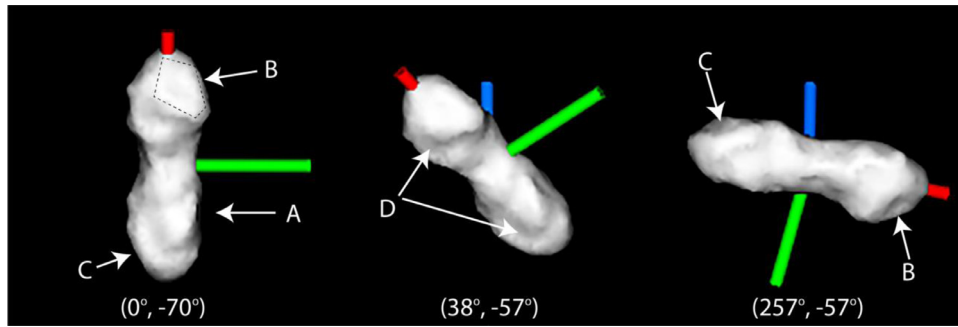


Fig. 6. Three views of our Kleopatra model to illustrate major shape features. The body-centered longitude and latitude view are listed below each model. The red (or shortest in the non-color reproduction) peg marks the major axis at 0° longitude and latitude; the green (longest) peg marks the intermediate axis at 90° longitude and 0° latitude (equatorial); and the blue peg (pointing away from the viewer) marks the spin axis at +90° latitude. Labeled arrows and the dashed polygon indicate features described in the text. (For interpretation of the references to color in this figure legend, the reader is referred to the web version of this article.)

Table 5
Kleopatra CW echo power spectra.

Epoch (UT)	SNR	Lon (°)	σ_{OC} (km ²)	Area (km ²)	$\hat{\sigma}_{OC}$	μ_c
18 Nov-01 Dec 1985 Sum	20	–	7,385	19,000	0.39	0.09 ± 0.04
1999 Sep 19 08:00	16	312	14,556	19,061	0.76	0.00
1999 Sep 19 08:51	13	255	9,963	19,464	0.51	0.00
1999 Sep 19 09:41	17	200	8,278	18,669	0.44	0.07
1999 Sep 20 08:10	9	138	11,325	18,996	0.60	0.28
1999 Sep 20 08:22	7	124	9,944	19,230	0.52	0.10
1999 Sum	28	–	10,192	19,084	0.53	0.00 ± 0.03
2008 Sep 19 04:18	13	23	1,649	10,127	0.16	0.11 ± 0.08
2013 Nov 11 05:01	90	55	5,935	18,680	0.32	0.03 ± 0.01

Epoch is the date and time of the mid-receipt of each run or the summed runs. Lon is the center longitude of the shape model at the time of each run. σ_{OC} is the OC radar cross-section in km². 1985 and 2013 data were at latitudes of –57°; the 1999 data were at latitude –67°; and the 2008 run was at –12° (Table 1). Area is the visible cross-sectional area of the shape model at the time of each run, or the average for summed runs. $\hat{\sigma}_{OC}$ is the radar albedo, the ratio of the previous two columns, and μ_c is the polarization ratio (see text). Uncertainties in radar albedo are 25%.

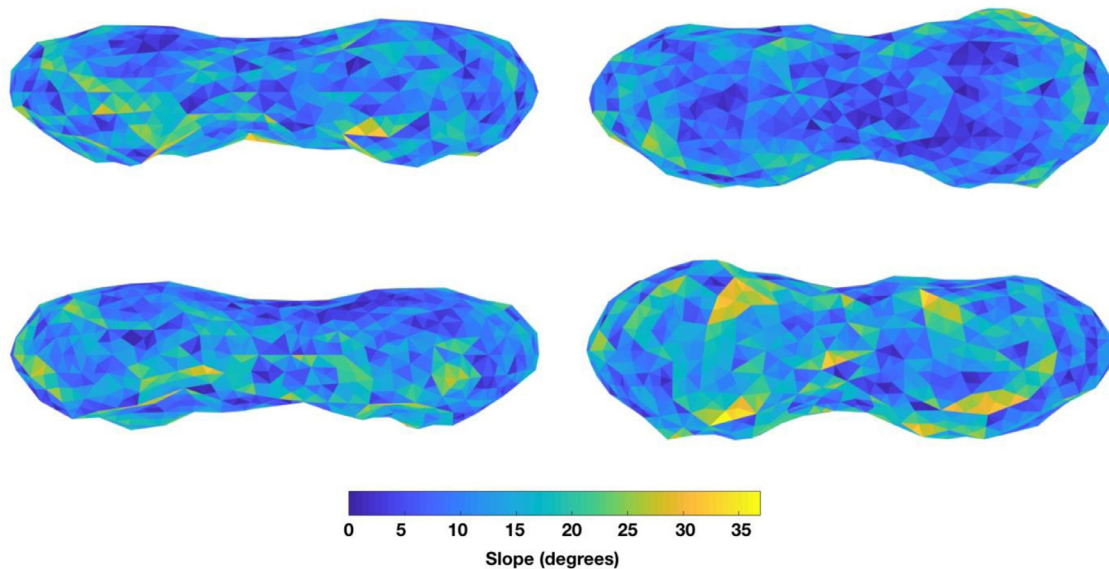


Fig. 7. Surface slopes over the Kleopatra shape, incorporating gravitational and rotational accelerations. The figure orientations are like those in Fig. 1 except the end-on views are not shown.

ure of equilibrium, and non-zero slopes imply friction angles for the surface covering.

Fig. 9 shows a measure of the surface geopotential across Kleopatra, computed accounting for both the constant density gravity field and the uniform rotation. The geopotential is measured in terms of speed a particle would gain from the highest point on the Kleopatra potential (at the zero regions) to

the lowest point in the neck region, on the order of 40 m/s (Scheeres et al., 2016). This should be compared with a characteristic circular orbit speed of approximately 71 m/s, and a maximum escape speed of 165 m/s (near the neck region) and a minimum escape speed of 49 m/s (at one of the long ends).

With this geopotential distribution, loose material on its surface will preferentially migrate towards the neck region of the body.

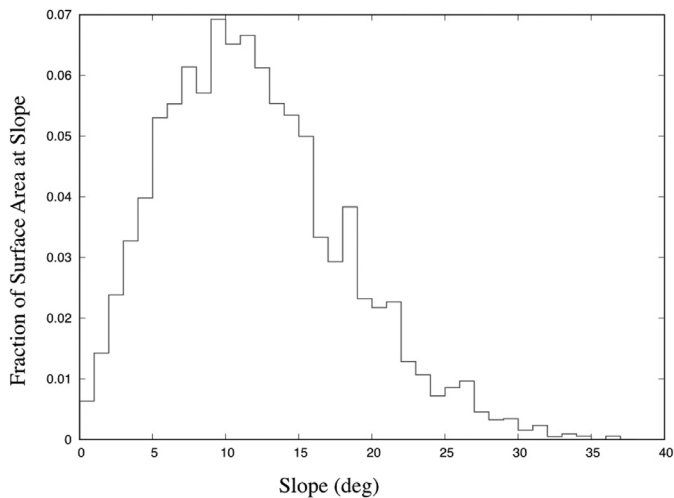


Fig. 8. Distribution of slopes angles over the Kleopatra body, with the fraction of the total surface area at a given slope indicated. The surface is largely relaxed, with a mean slope angle of 12° .

The low surface slopes across the body indicate that the surface is relatively relaxed, implying that surface migration may have already occurred in the past. Our radar observations (Fig. 2) support this hypothesis. Our shape model simulations assume a ho-

mogeneous radar reflectivity but, in the radar images (Fig. 2 left columns), the neck is often absent or darker than predicted by the simulations (Fig. 2 center columns), consistent with the presence of a thicker layer of loose material there. The migration of loose material may also play a role in Kleopatra's lower than expected radar albedo at equatorial aspects.

5. Next opportunities and model availability

The next opportunities to observe Kleopatra at Arecibo (the only radar observatory currently capable of this) occur in Aug 2022, when it will be at an equatorial aspect (similar to the 2008 observations), and in Nov 2027 when it will be at an aspect of -60° , similar to that of the 2013 observations. The 2022 encounter will allow us to verify the lower radar albedo observed in 2008. During both encounters, the SNR will be high enough for delay-Doppler imaging and allow further refinements to the shape model.

There are numerous opportunities to observe Kleopatra occult a star in the near future. Four opportunities are listed for the latter half of 2018 and early 2019 in Table 6. Fig. 10 shows the geographic region where each occultation is visible and the associated plane-of-sky appearance expected for Kleopatra from our model. Dense coverage of the 2018 November and December occultations would be especially valuable for constraining its major and minor axes as the asteroid will appear nearly broadside at a sub-observer latitude of -36° .

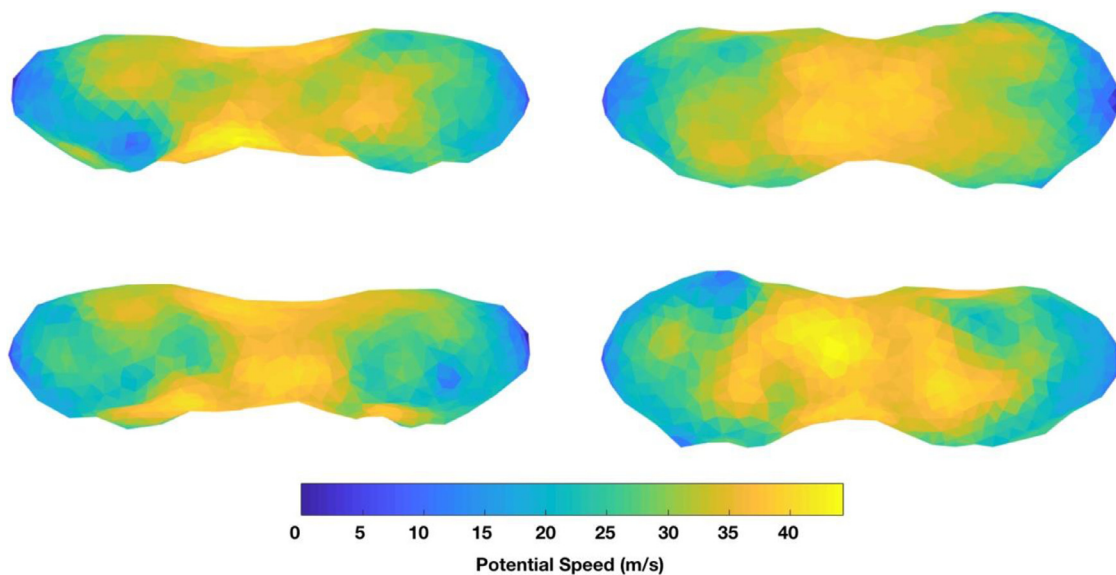


Fig. 9. A measure of the geopotential across the surface of Kleopatra. The values indicate the speed that would be attained by a particle move from the highest point in the potential (at the ends of the body) to the lowest point in the neck region. The figure orientations are the same as given in Fig. 7 and like Fig. 1 except the end-on views are not shown.

Table 6

Future occultations of Kleopatra.

Date (UT)	Time (UT)	Location	RA, DEC	Lon (deg)	Duration (s)	Star Mv	Mag Drop
28 Oct 2018	08:34	S Canada, NE USA	113,+9	158	10.2	11.2	0.9
07 Nov 2018	01:16	C Europe, Saudi Arabia	115,+7	81	13.3	12.0	0.5
07 Dec 2018	02:36	S. America, UK	115,+3	95	18.5	10.6	0.9
06 Jan 2019	12:50	N Australia	109,+1	232	12.9	11.1	0.5

Date and Time refer to the approximate median time for observations.

Location is the geographic region where the occultation is visible.

RA,DEC is the Right Ascension and declination of the star to be occulted.

Lon is the center longitude of Kleopatra at the reported time; Lon of 90° or 270° would be broadside.

All of these occultations are at a sub-observer aspect (latitude) of $-36^\circ \pm 2^\circ$

Duration is the expected duration of the occultation.

Star Mv is the visual magnitude of the occulted star.

Mag drop is the expected drop in Mv during the occultation.

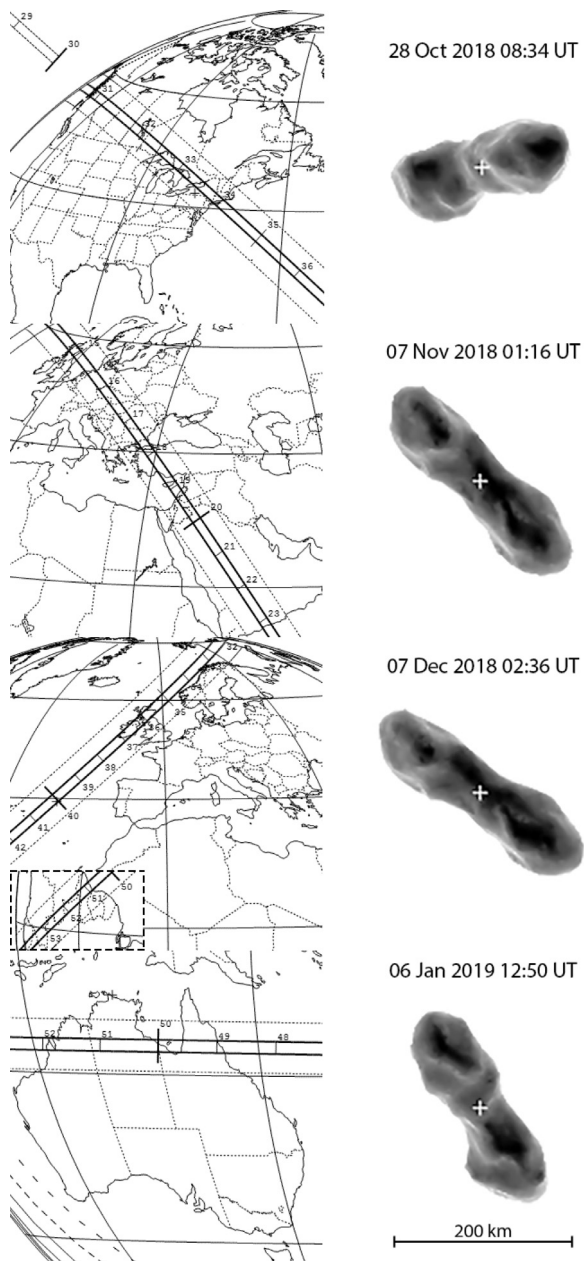


Fig. 10. Four future occultation opportunities for Kleopatra. The left panels show the projected geographic centerline of the expected occultation, and the right show the respective model projected plane-of-sky view. The first three occultations occur over densely populated areas and offer the best prospects for multiple chord coverage. The 2018 November and December occultations will be especially valuable for constraining Kleopatra's size and shape in a nearly full-breadth view.

This revised Kleopatra model is now available at the Jet Propulsion Laboratory Asteroid Radar Research web page (echo.jpl.nasa.gov) for others who wish to conduct additional research on this fascinating object.

Acknowledgements

This paper is dedicated to the thousands of active amateur astronomers who labor in near anonymity and yet often provide critically important observations. The work presented here would not have been possible without the five stellar occultations recorded by several dozen of them. The contributions of Steven J. Ostro (1946–2008) to this work are also gratefully acknowledged. We thank

J. Hanus for providing the AO images used in our Fig. 5, and B. Carry and an anonymous reviewer for their thoughtful comments. Finally, we are grateful to the staff at Arecibo Observatory for their work and dedication to the field of planetary astronomy. We wish them and the people of Puerto Rico a swift recovery from Hurricane Maria.

The Arecibo Observatory is operated by SRI International under a cooperative agreement with the National Science Foundation (AST-1100968), and in alliance with Ana G. Méndez-Universidad Metropolitana, and the Universities Space Research Association. The Arecibo Planetary Radar Program is supported by the National Aeronautics and Space Administration under Grant no. NNX12AF24G issued through the Near Earth Object Observations program.

Parts of this work was performed at the Jet Propulsion Laboratory, California Institute of Technology, under contract with the National Aeronautics and Space Administration. This material is based in part upon work supported by the National Aeronautics and Space Administration (NASA) under the Science Mission Directorate Research and Analysis Programs.

Appendix A

See Table A.1

Table A.1
Occultation observers.

1980
S. Krysko
G. Stokes
Beals/Belcher/Loehde.
D. Scarlett
Jones/Bowen
D. Hube
G. Fouts
Mitchell
E. Mannery
1991
D. Dunham
W. Warren
J. Guerber
C. Aikman
M. Fletcher
R. Mordic
S. Storch
J. Pyral
E. Lurcott
M. Henry
J. Fox
R. Bolster
D. Grieser
2009
D. Dunham
J. Ray
R. Peterson
P. Maley
G. Rattley
S. Degenhardt
L. Martinez
J. Stamm
2015
H. Bulder
F. Dorst
O. Kloes
J-M. Winkel
O. Farago
V. Metallinos
H. Rutten
H. De Groot

(continued on next page)

Table A.1 (continued)

B. Gaehrken
 H. Kostense
 D. Fischer
 H. Purucker
 R. Stoyan
 E. Bredner
 A. Mueller
 L. Blommers
 K. Moddemeijer
 P. Bastiaansen
 W. Nobel
 C. Sauter
 M. Devogele
 M. Kohl
 J. De Queiroz
 K-L Bath
 M. Federspiel
 F. Emering
 F. Van Den Abbeel
 R. Bourtembourg
 J. Schenker
 J. Lecacheux
 E. Meza
 S. Sposetti
 R. Di Luca
 T. Pauwels
 P. De Cat
 C. Demeautis
 D. Matter
 A. Manna
 A. Ossola
 C. Gualdoni
 R. Decellier
 F. Ciabattar
 M. Bachini
 G. Bonatti
 A. Pratt
 G. Sautot
 R. Boninsegnax
 F. Delucchi
 M. Federspiel
 G. Sautot
 E. Vauthrin
 O. Dechambre
 J. Berthier
 F. Vachier
 B. Carry
 M. Pajuelo
 J. Rovira
 2016
 B. Dunford
 A. Olsen
 D. Dunham
 J. Dunham
 N. Smith
 R. Venable
 S. Messner

- Carry, B., 2012. Density of asteroids. *Planet Space Sci* 73, 98–118.
- Chapman, C.R., Salisbury, J.W., 1973. Comparisons of meteorite and asteroid spectral reflectivities. *Icarus* 19, 507–522.
- Demura, H., Kobayashi, S., Nemoto, E., Matsumoto, N., Furuya, M., Yukishita, A., Muranaka, N., Morita, H., Shirakawa, K., Maruya, M., Ohyama, H., Uo, M., Kubota, T., Hashimoto, T., Kawaguchi, J., Fujiwara, A., Saito, J., Sasaki, S., Miyamoto, H., Hirata, N., 2006. Pole and global shape of 25143 Itokawa. *Science* 312, 1347–1349.
- Descamps, P., Marchis, F., Berthier, J., Emery, J.P., Duchêne, G., de Pater, I., Wong, M.H., Lim, L., Hammel, H.B., Vachier, F., Wiggins, P., Teng-Chuen-Yu, J.-P., Peyrot, A., Pollock, J., Assafin, M., Vieira-Martins, R., Camargo, J.I.B., Braga-Ribas, F., Macomber, B., 2011. Triplicity and physical characteristics of asteroid (216) Kleopatra. *Icarus* 211, 1022–1033.
- Descamps, P., 2015. Dumb-bell-shaped equilibrium figures for fiducial contact-binary asteroids and EKBOs. *Icarus* 245, 64–79.
- Dunham, D.W., Herald, D., Frappa, E., Hayamizu, T., Talbot, J., Timerson, B., 2016. Asteroid Occultations V14.0 NASA Planetary Data System, id. EAR-A-3-RDR-OCULTATIONS-V14.0 NASA ADS entry: <http://adsabs.harvard.edu/abs/2016PDSS..243.....D>.
- Durech, J., Sidorin, V., Kaasalainen, M., 2010. DAMIT: a database of asteroid models. *Astron & Astrophys* 513, id. A46 13pp. doi: 10.1051/0004-6361/200912693.
- Gaffey, M.J., 1976. Spectral reflectance characteristics of the meteorite classes. *J. Geophys. Res.* 81, 905–920.
- Gaffey, M.J., McCord, T.B., 1979. Mineralogical and petrological characterizations of asteroid surface materials. In: Gehrels, T. (Ed.), *Asteroids*. University of Arizona Press, Tucson, pp. 688–723.
- Hanuš, J., Viikinkoski, M., Marchis, F., Durech, J., Kaasalainen, M., Delbo', M., Herald, D., Frappa, E., Hayamizu, T., Kerr, S., Preston, S., Timerson, B., Dunham, D., Talbot, J., 2017. Volumes and bulk densities of forty asteroids from ADAM shape modeling. *A&A* 601, id.A114. doi: 10.1051/0004-6361/201629956.
- Harmon, J.K., 2002. Planetary delay-Doppler radar and the long-code method. *IEEE Trans. Geosci. Remote Sens.* 40, 1904–1916.
- Hirabayashi, M., Scheeres, D.J., 2014. Analysis of asteroid (216) Kleopatra using dynamical and structural constraints. *Astron. Astrophys. J.* 780, 160. doi:10.1088/0004-637X/780/2/160.
- Herstroffer, D., Bertier, J., Descamps, P., Tanga, P., Cellino, A., Lattanzi, M., DiMartino, M., Zappala, V., 2002a. Asteroid (216) Kleopatra: tests of the radar-derived shape model. *Astron. Astrophys.* 392, 729–733.
- Herstroffer, D., Marchis, F., Fusco, T., Berthier, J., 2002b. Adaptive optics observations of asteroid (216) Kleopatra. *Astron. Astrophys.* 394, 339–343.
- Kaasalainen, M., Viikinkoski, M., 2012. Shape reconstruction of irregular bodies with multiple complementary data sources. *Astron. Astrophys.* 543 (A97), 9.
- Magri, C., Nolan, M.C., Ostro, S.J., Giorgini, J.D., 2007a. A radar survey of main-belt asteroids: Arecibo observations of 55 object during 1999–2003. *Icarus* 186, 126–151.
- Magri, C., Ostro, S.J., Scheeres, D.J., Nolan, M.C., Giorgini, J.D., Benner, L.A.M., Margot, J.L., 2007b. Radar observations and a physical model of Asteroid 1580 Betulia. *Icarus* 186, 152–177.
- Mainzer, A., Grav, T., Bauer, J., Masiero, J., McMillan, R.S., Cutri, R.M., Walker, R., Wright, E., Eisenhardt, P., Tholen, D.J., Spahr, T., Jedicke, R., Denneau, L., DeBaun, E., Elsbury, D., Gautier, T., Gomillion, S., Hand, E., Mo, W., Watkins, J., Wilkins, A., Bryngelson, G.L., Del Pino Molina, A., Desai, S., Gómez Camus, M., Hidalgo, S.L., Konstantopoulos, I., Larsen, J.A., Maleszewski, C., Malkan, M.A., Mauduit, J.C., Mullan, B.L., Olszewski, E.W., Pforr, J., Saro, A., Scotti, J.V., Wasserman, L.H., 2011. Preliminary Results from NEOWISE: An Enhancement of the Wide-field Infrared Survey Explorer for Solar System Science. *The Astrophysical Journal* 731 (1), 13. article id. 53. <http://adsabs.harvard.edu/abs/2011ApJ...743..156M>.
- Marchis, F., Descamps, P., Berthier, J., Emery, J.P., 2008. S/2008 ((216)) 1 AND S/2008 ((216)) 2. *IAU Circ.*, No. 8980, #1. <http://adsabs.harvard.edu/abs/2008IAUC.8980...1M>.
- Marchis, F., Descamps, P., Berthier, J., Vachier, F., Emery, J.P., 2010. Minor Planet Circular, No. 73983, 02/2011, https://minorplanetcenter.net/iau/ECS/MPCArchive/2011/MPC_20110218.pdf.
- Marchis, F., Enriquez, J.E., Emery, J.P., Mueller, M., Baek, M., Pollock, J., Assafin, M., Vieira Martins, R., Berthier, J., Vachier, F., Cruikshank, D.P., Lim, L.F., Reichart, D.E., Ivarsen, K.M., Haislip, J.B., LaCluyze, A.P., 2012. Multiple asteroid systems: Dimensions and thermal properties from Spitzer Space Telescope and ground-based observations. *Icarus* 221 (2), 1130–1161. <http://adsabs.harvard.edu/abs/2012Icar..221.1130M>.
- Marchis, F., Herstroffer, D., Cellino, A., Tanga, P., Zappala, V., 1999. (216) Kleopatra. *IAU Circ.*, No. 7308, #1. <http://adsabs.harvard.edu/abs/1999IAUC.7308...1M>.
- Merline, W.J., Close, L.M., Dumas, C., et al. 2000. AAS/Division Planet. Sci. Meet., 32, 1306.
- Mitchell, D.L., Ostro, S.J., Rosema, K.D., Hudson, R.S., Campbell, D.B., Chandler, J.F., Shapiro, I.I., 1995. Radar observations of 7 Iris, 9 Metis, 12 Victoria, 216 Kleopatra, and 654 Zelinda. *Icarus* 118, 105–131.
- Ostro, S.J., Hudson, R.S., Nolan, M.C., Margot, J.-L., Scheeres, D.J., Campbell, D.B., Magri, C., Giorgini, J.D., Yeomans, D.K., 2000. Radar observations of asteroid 216 Kleopatra. *Science* 288, 836–839.
- Ostro, S.J., Hudson, R.S., Benner, L.A.M., Giorgini, J.D., Magri, C., Margot, J.L., Nolan, M.C., 2002. Asteroid radar astronomy. In: Bottke, Jr., W.F., Cellino, A., Paolicchi, P., Binzel, R.P. (Eds.), *Asteroids III*. University of Arizona, Tucson, pp. 151–168.
- Scheeres, D.J., 2012. *Orbital Motion in Strongly Perturbed Environments: Applications to Asteroid, Comet and Planetary Satellite Orbiters* ISBN 978-3-642-03255-4.

Supplementary materials

Supplementary material associated with this article can be found, in the online version, at doi:10.1016/j.icarus.2018.04.002.

References

- Bell, J.F., Davis, D.R., Hartmann, W.K., Gaffey, M.J., 1989. Asteroids: the big picture. In: Binzel, R.P., Gehrels, T., Matthews, M.S. (Eds.), *Asteroids II*. University of Arizona, Tucson, pp. 921–948.
- Benner, L.A.M., Ostro, S.J., Magri, C., Nolan, M.C., Howell, E.S., Giorgini, J.D., Jurgens, R.F., Margot, J.L., Taylor, P.A., Busch, M.W., Shepard, M.K., 2008. Near-Earth asteroid surface roughness depends on compositional class. *Icarus* 198, 294–304. <http://adsabs.harvard.edu/abs/2008Icar..198..294B>.
- Britt, D.T., Consolmagno, G.J., 2001. Stony meteorite porosities and densities: a review of the data through 2001. *Meteorit. Planet. Sci.* 38, 1161–1180.
- Campbell, D.B., Davis, M.M., Goldsmith, P.F., Perillat, P.J., 1997. The new Arecibo Telescope: Status and performance. American Astronomical Society, 191st meeting, 57.01, *Bull. AAS* 29, 1305.

- Scheeres, D.J., Hesar, S.G., Tardivel, S., Hirabayashi, M., Farnocchia, D., McMahon, J.W., Chesley, S.R., Barnouin, O., Binzel, R.P., Bottke, W.F., Daly, M.G., Emery, J.P., Hergenrother, C.W., Lauretta, D.S., Marshall, J.R., Michel, P., Nolan, M.C., Walsh, K.J., 2016. The geophysical environment of Bennu. *Icarus* 276, 116–140.
- Shepard, M.K., Taylor, P.A., Nolan, M.C., Howell, E.S., Springmann, A., Giorgini, J.D., Warner, B.D., Harris, A.W., Stephens, R., Merline, W.J., Rivkin, A., Benner, L.A.M., Coley, D., Clark, B.E., Ockert-Bell, M., Magri, C., 2015. A radar survey of M- and X-class asteroids. III. Insights into their composition, hydration state, and structure. *Icarus* 245, 38–55.
- Shepard, M.K., Richardson, J., Taylor, P.A., Rodriguez-Ford, L.A., Conrad, A., de Pater, I., Adamkovic, M., de Kleer, K., Males, J.R., Morzinski, K.M., Close, L.M., Kaasalainen, M., Viikinkoski, M., Timerson, B., Reddy, V., Magri, C., Nolan, M.C., Howell, E.S., Benner, L.A.M., Giorgini, J.D., Warner, B.D., Harris, A.W., 2017. Radar observations and shape model of asteroid 16 Psyche. *Icarus* 281, 288–403.
- Szabo, G.M., Kiss, L., 2008. The shape distribution of asteroid families: evidence for evolution driven by small impacts. *Icarus* 196, 135–143.
- Tanga, P., Hestroffer, D., Berthier, J., Cellino, A., Lattanzi, G., DiMartino, M., Zapala, V., 2001. HST/FGS observations of the asteroid (216) Kleopatra. *Icarus* 153, 451–454.
- Tedesco, E.F., Noah, P.V., Noah, M., 2002. The supplemental IRAS minor planet survey. *Astron. J.* 123, 1056–1085.
- Usui, F., Kuroda, D., Müller, T.G., Hasegawa, S., Ishiguro, M., Ootsubo, T., Ishihara, D., Kataza, H., Takita, S., Oyabu, S., Ueno, M., Matsuhara, H., Onaka, T., 2011. Asteroid catalog using Akari: AKARI/IRC mid-infrared asteroid survey. *Publ. Astron. Soc. Jpn.* 63, 1117–1138.
- Vernazza, P., Lamy, P., Groussin, O., Hiroi, T., Jorda, L., King, P.L., Izaw, M.R.M., Marchis, F., Birlan, M., Brunetto, R., 2011. Asteroid (21) Lutetia as a remnant of Earth's precursor planetesimals. *Icarus* 216, 650–659.